Bayesian Approach for a Robust Speed-of-Sound Reconstruction Using Pulse-Echo Ultrasound

Patrick Stähli, Martin Frenz, *Member, IEEE*, and Michael Jaeger

Abstract—Computed ultrasound tomography in echo mode (CUTE) is a promising ultrasound (US) based multi-modal technique that allows to image the spatial distribution of speed of sound (SoS) inside tissue using hand-held pulse-echo US. It is based on measuring the phase shift of echoes when detected under varying steering angles. The SoS is then reconstructed using a regularized inversion of a forward model that describes the relation between the SoS and echo phase shift. Promising results were obtained in phantoms when using a Tikhonov-type regularization of the spatial gradient (SG) of SoS. In-vivo, however, clutter and aberration lead to an increased phase noise. In many subjects, this phase noise causes strong artifacts in the SoS image when using the SG regularization. To solve this shortcoming, we propose to use a Bayesian framework for the inverse calculation, which includes *a priori* statistical properties of the spatial distribution of the SoS to avoid noise-related artifacts in the SoS images. In this study, the *a priori* model is based on segmenting the B-Mode image. We show in a simulation and phantom study that this approach leads to SoS images that are much more stable against phase noise compared to the SG regularization. In a preliminary in-vivo study, a reproducibility in the range of 10 ms^{-1} was achieved when imaging the SoS of a volunteer's liver from different scanning locations. These results demonstrate the diagnostic potential of CUTE for example for the staging of fatty liver disease.

Index Terms—Ultrasound tomography, reflection mode, multimodal imaging, inverse problem.

I. INTRODUCTION

CLASSICAL gray scale B-Mode ultrasound (US) determines the tissue's echogenicity and displays it in a spatially resolved way. In that way, it allows the evaluation of various traumatic and pathologic conditions and is therefore routinely used in today's clinical diagnostic practice. However, US often suffers from non-specific contrast and low sensitivity for certain disease types [1]–[3]. To improve its diagnostic accuracy, much effort has been placed in recent years in developing new ultrasound-based multi-modal approaches that complement classical gray scale B-Mode images with additional functional and structural information [4]–[13].

Speed-of-sound (SoS) imaging is a promising candidate to further improve US based diagnosis. It allows the identification of disease-related alterations of tissue composition and structure, based on their influence on the speed at which US propagates through tissue. SoS imaging can be divided into two categories: through-transmission and reflection mode imaging. Through-transmission techniques reconstruct the spatial distribution of SoS by analysing US transmitted through the tissue from various different angles. Breast ultrasound tomography demonstrates impressively the diagnostic potential of through transmission SoS imaging on the example of breast cancer diagnosis [14]–[17]. Although breast UCT yields quantitative SoS images with high spatial and contrast resolution, it requires a bulky stand-alone system and an acoustically transparent target, which limits it's application mainly to the female breast, even though its use has recently been demonstrated for orthopedic and myopatic imaging of the leg [18].

In contrast, SoS imaging in reflection mode has the advantage that it provides all the flexibility of conventional US. Thus, implementation in a state-of-the art equipment would allow to image the SoS distribution in any part of the human body. Therefore, it could extend the applicability of SoS imaging to e.g the diagnosis of cancer other than in the breast, the assessment of fatty liver disease, or the characterization of plaque composition inside large blood vessels. Various approaches that estimate the spatial distribution of SoS based on pulse-echo signals have been investigated so far [19]–[25]. Quantitative reflection mode determination of average SoS (as opposed to imaging) has been demonstrated in the liver in vivo [26], proving the diagnostic value of SoS in the example of fatty liver disease [27].

We have developed a reflection-mode technique called computed ultrasound tomography in echo mode (CUTE) that allows handheld imaging of the spatial distribution of SoS in real time [28]. The working principle of CUTE is as follows: radio-frequency (rf) mode US images are beamformed

(using e.g. conventional delay-and-sum algorithm) under a set of various different transmit (Tx) and receive (Rx) angles [29]. The deviation of the true SoS from the SoS that is assumed for beamforming results in a mismatch between the actual and anticipated round trip time of US propagation (henceforth termed 'aberration delay'). Detecting echoes under varying angles of US transmission and reception leads to a changing value of the aberration delay which is in turn reflected in a phase shift of the detected echos in between the images acquired with the different sets of Tx and Rx angle combinations. This phase shift can be quantified in a spatially resolved way by using e.g. Loupas or Kasai type phase correlation [30], [31]. A forward model [29] relates these measured echo-phase shifts to the spatial distribution of local SoS, which can be derived by solving the inverse problem. One of the difficulties that arises when solving such inverse problems is that small variations in the inputs (e.g. caused by measurement noise) can cause large changes in the solution [32]. To stabilize the solution, some sort of regularization must be included in the inverse problem formulation to give preference to a particular solution with desirable properties, where the meaning of desirable properties is defined *a priori*. A Tikhonov type regularization of the spatial gradient (SG) of SoS was used in previous studies [29], [33], based on the expectation that the distribution of SoS inside a tissue is smooth and does not vary strongly on a short spatial scale. Promising results were achieved in phantom studies using this technique [29]. In-vivo, however, clutter and aberration often lead to an increased phase noise compared to phantoms, resulting in detrimental artifacts. Even worse, since the spatial distribution of this phase noise changes when changing the transducer position, it not only leads to a high level of artifacts in the SoS images, but also limits the reproducibility when imaging an organ (e.g. the liver) from different scanning locations. To solve this shortcoming, we propose to use a Bayesian framework for the inverse calculation, as frequently applied in geophysical inverse theories [32], [34]–[37]. One of the advantages of the Bayesian framework is that it provides an intuitive and practical way to include a physically motivated *a priori* statistical model about the distribution of SoS into the formulation of the inverse calculation. Promising results have been reported using this approach in US through-transmission tomography, where it improves axial resolution when only a limited set of angles are available [38].

In this study, the *a priori* information is derived from the B-Mode images and encoded in a covariance matrix that gives a statistical description of the range and spatial correlation of the expected spatial distribution of SoS. This covariance matrix then acts as a regularization term to stabilize the solution of the inverse problem. It turns out that this approach makes the SoS reconstruction less prone to noise and thus leads to more reproducible SoS images compared to the SG regularization.

Building on [39], this study evaluates and compares the performance of both regularization approaches in simulation as well as phantom experiments. In preparation of one of our target clinical applications, and to demonstrate the benefit of the Bayesian approach also in-vivo, the regularization techniques
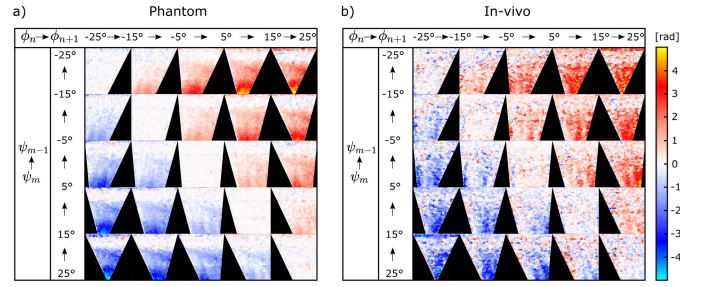

Fig. 1. Exemplary echo-phase shift maps determined between angle combinations (Tx: $\phi_n \rightarrow \phi_{n+1}$, Rx: $\psi_m \rightarrow \psi_{m-1}$) for angles (ϕ, ψ) ranging from -25° to 25° in 10° steps for (a) a phantom mimicking the abdominal wall and liver tissue (see Fig. 4a) and (b) imaging the liver through the abdominal wall for a healthy volunteer (scanning location A, see Fig. 4b). The phase shift tracking covered a range of 40 × 40 mm for each angle combination. The black areas represent areas of missing data due to the limited aperture size of the probe.

are also compared in an exemplary in-vivo scenario, imaging the abdominal wall and liver tissue of a healthy volunteer.

II. MATERIALS AND METHODS

As in our previous study [29], CUTE was implemented using plane-wave pulse-echo rf-data that are acquired and beamformed (using delay-and-sum together with coherent plane-wave compounding) for a set of various different transmit (Tx) and receive (Rx) angles. Applying the common-mid-angle approach with the same experimental parameters as outlined in [29], maps of local echo-phase shift are then determined between angle combinations (Tx: $\phi_n \rightarrow \phi_{n+1}$, Rx: $\psi_m \rightarrow \psi_{m-1}$) for angles (ϕ, ψ) ranging from -25° to 25° in 10° steps.

For illustration, Fig. 1 shows the echo-phase shift maps determined in a phantom mimicking the abdominal wall and liver tissue (see section II-D, Phantom C) and when imaging the liver of a healthy volunteer through the abdominal wall (see section III-C, scanning location A). Due to the similarity of the spatial distribution of SoS between the phantom and the in-vivo scenario, also the phase shift maps look similar. However, the phase shift maps determined in-vivo are contaminated by a higher level of phase noise.

The SoS is reconstructed by relating – via a forward model **M** – the vectorized echo phase shift maps $\Delta\Theta$ to the vectorized distribution of slowness deviation Δs, i.e. the difference between the actual slowness (inverse SoS) $1/c$ and the reference slowness $1/c_0$ that is used for beamforming. This forward model, which is described in detail in our previous study [29], is based on a geometric perspective (see Fig. 2a). We assume a reflector that is detected under a specific angle pair (ϕ_n, ψ_m). The mismatch between the actual and anticipated (for beamforming) round trip time of US propagation leads to an offset d of the reconstructed position of the echo, away from the true location of the reflector along a direction determined by the mid-angle γ. This offset d is given by:

$$d(\phi, \psi) = \frac{c_0 \left[\tau_{tx}(\mathbf{r}, \psi_n) + \tau_{rx}(\mathbf{r}, \psi)\right]}{2\cos\left[\frac{1}{2}(\phi_n - \psi_n)\right]} \quad (1)$$

a) b)
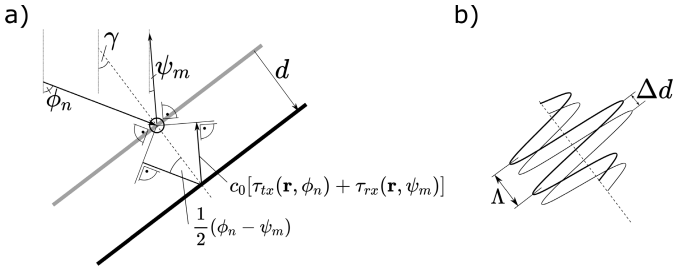
Fig. 2. (a) Sketch showing the relation between the Tx/Rx angle pair, the aberration delays τ and the spatial offset d between the true position of the reflector and the reconstructed position. (b) The measured phase shift is determined by the ratio between the difference of the offset of the echo and the spatial period Λ. This figure is adapted from [29], licensed under a Creative Commons Attribution 4.0 International licence (https://creativecommons.org/licenses/by-nc-nd/4.0CC BY-NC-ND 4.0).

When changing the angle combination (ϕ_n, ψ_m) to (ϕ_{n+1}, ψ_{m-1}), this offset changes accordingly. As illustrated in Fig. 2b, the phase shift is then the ratio between the difference of the offsets Δd and the spatial period Λ. When Λ is fixed by filtering to a value $\Lambda = c_0/(2 f_0)$ independent on ϕ and ψ, this ratio reads:

$$\Delta \Theta(\mathbf{r}, \phi_n, \phi_{n+1}, \psi_m, \psi_{m-1}) \simeq \frac{2\pi \Delta d}{\Lambda}$$

$$= 2\pi f_0 \left\{ \frac{\tau_{tx}(\mathbf{r}, \phi_n) + \tau_{rx}(\mathbf{r}, \psi_m)}{\cos\left[\frac{1}{2}(\phi_n - \psi_m)\right]} \right.$$

$$\left. - \frac{\tau_{tx}(\mathbf{r}, \phi_{n+1}) + \tau_{rx}(\mathbf{r}, \psi_{m-1})}{\cos\left[\frac{1}{2}(\phi_{n+1} - \psi_{m-1})\right]} \right\} \quad (2)$$

where f_0 denotes the center frequency, and the aberration delays τ_{tx} and τ_{rx} are the excess propagation delays due to deviations of the SoS from the *a priori* value. Note that, as a consequence of explicitly modelling the reconstruction position error, this relation contains an inverse cosine law which was not taken into account by some of the previous studies. We have shown in [29] that this inverse cosine law is a prerequisite for accurate quantitative SoS reconstruction. Assuming that the sound propagation follows the straight-ray approximation, τ_{tx} and τ_{rx} are related to the line integrals of slowness deviation Δs, along the steering angles ϕ and ψ.

$$\tau_{tx,rx}(\mathbf{r}, \phi, \psi) = \int_{\phi, \psi}^{\mathbf{r}} dl \left\{ \frac{1}{c(\mathbf{r})} - \frac{1}{c_0(\mathbf{r})} \right\} \equiv \int_{\phi, \psi}^{\mathbf{r}} dl \, \Delta s(\mathbf{r})$$

$$(3)$$

Thanks to the straight-ray approximation, the forward model $\mathbf{M}$ is linear and can thus be formulated in matrix notation:

$$\Delta \Theta = \mathbf{M} \Delta s + \epsilon \quad (4)$$

ϵ describes the measurement noise that contaminates the echo-phase shift maps as indicated in Fig. 1. In the following, two different approaches are described and investigated that estimate Δs based on Eq. 4.

A. SoS Reconstruction Based on Spatial Gradient Regularization

Since $\mathbf{M}$ is poorly-conditioned and $\Delta \Theta$ steadily contaminated by noise, Eq. 4 is not expected to have an exact solution.

Instead, an objective function $L(\Delta s)$ via the squared L2 norm of the residuals is formulated:

$$L(\Delta s) = \|\Delta \Theta - \mathbf{M} \Delta s\|_2^2 + \|\mathbf{T} \Delta s\|_2^2 \quad (5)$$

The second term on the right-hand side of the Eq. 5 denotes the regularization term that prevents the estimated slowness deviation to be unduly sensitive to noise-related variations in the measurement data vector $\Delta \Theta$. By minimizing the objective function $L(\Delta s)$, it follows that the estimated slowness deviation $\widehat{\Delta s}$ is given by:

$$\widehat{\Delta s} = \left(\mathbf{M}^T \mathbf{M} + \mathbf{T}^T \mathbf{T} \right)^{\text{inv}} \mathbf{M}^T \Delta \Theta \quad (6)$$

The estimated SoS $\hat{c}$ is finally recovered from the estimated slowness deviation $\widehat{\Delta s}$ according to:

$$\hat{c} = \left(\widehat{\Delta s} + \frac{1}{c_0} \right)^{-1} \cong c_0 - c_0^2 \widehat{\Delta s} \quad (7)$$

where c_0 designates the anticipated SoS that is used for beamforming. In this study, c_0 is set to 1540 ms^{-1} for all experiments.

In line with previous studies [29], [33], the regularization matrix $\mathbf{T}$ is based on finite difference operators $\mathbf{D}$ in x and z direction with independent regularization parameters γ_x and γ_y:

$$\mathbf{T} = \begin{bmatrix} \gamma_x \mathbf{D}_x \\ \gamma_z \mathbf{D}_z \end{bmatrix} \quad (8)$$

The finite difference regularization enforces a smooth slowness profile of the to-be reconstructed slowness without imposing a constraint on the mean slowness.

B. SoS Reconstruction Using a priori Knowledge

Whereas the previously described parameter estimation of Δs was based on a purely algebraic framework, it can also be derived based on a Bayesian interpretation of the forward problem, as has been thoroughly developed in [32] and described in great detail in [40]. Based on Bayes' theorem, the posterior probability density $P(\Delta s | \Delta \Theta)$ is the probability of the parameters Δs given the evidence $\Delta \Theta$:

$$P(\Delta s | \Delta \Theta) \propto P(\Delta s) P(\Delta \Theta | \Delta s) \quad (9)$$

In this study, a Gaussian *a priori* probability distribution $P(\Delta s)$ that is centred upon a mean value Δs_p with a covariance matrix $\mathbf{C}_M$ is assumed.

$$P(\Delta s) \propto \exp\left[-\frac{1}{2} (\Delta s - \Delta s_p)^T \mathbf{C}_M^{-1} (\Delta s - \Delta s_p) \right] \quad (10)$$

Further, it is assumed that the noise ϵ is also Gaussian in form with a covariance matrix $\mathbf{C}_N$, centred upon the prediction of the forward model.

$$P(\Delta \Theta | \Delta s) \propto \exp\left[-\frac{1}{2} (\Delta \Theta - \mathbf{M} \Delta s)^T \mathbf{C}_N^{-1} (\Delta \Theta - \mathbf{M} \Delta s) \right]$$

$$(11)$$

It is then possible to show that the posterior probability distribution for the model parameters Δs is [40]:

$$P(\Delta s | \Delta \Theta) \propto \exp\left[-\frac{1}{2} (\Delta s - \widehat{\Delta s})^T \hat{\mathbf{C}}^{-1} (\Delta s - \widehat{\Delta s}) \right] \quad (12)$$

where $\hat{\mathbf{C}}$ denotes the posterior covariance matrix.

$$\hat{\mathbf{C}} = \left(\mathbf{M}^T \mathbf{C}_N^{-1} \mathbf{M} + \mathbf{C}_M^{-1}\right)^{-1} \tag{13}$$

Since the posterior distribution is Gaussian, the most likely solution to the inverse problem is given by the mean of the posterior distribution $\widehat{\Delta \mathbf{s}}$:

$$\widehat{\Delta s} = \Delta s_p + \hat{\mathbf{C}} \mathbf{M}^T \mathbf{C}_N^{-1} (\Delta \Theta - \mathbf{M} \Delta s_p) \tag{14}$$

The estimation of the slowness deviation in Eq. 14 allows to conveniently include statistical *a priori* knowledge. Uncertainties associated with the forward modelling procedure (e.g. model discretization errors or uncertainties in the data as e.g. ambient noise) can in principle be included in the noise covariance matrix $\mathbf{C}_N$. In this study, however, we assume that the forward model has no uncertainties and that the ambient noise is uncorrelated. This leads to $\mathbf{C}_N$ being a diagonal matrix with all diagonal elements equal to an identical value σ_N^2 that describes the noise level in the data.

Δs_p denotes the *a priori* mean of the slowness deviation Δs. In this study, we assume that Δs_p is 0 everywhere, i.e. the *a priori* favored solution for the SoS is equal to c_0.

The covariance matrix $\mathbf{C}_M$ allows to include a statistical *a priori* model about the inter-pixel correlation of SoS. Such *a priori* knowledge can be derived from the B-Mode image that is reconstructed in parallel to CUTE. To generate the covariance matrix $\mathbf{C}_M$, the B-Mode image is in a first step segmented into N regions within which a correlation of the SoS is expected. In the present study this segmentation is performed by visual inspection. For example, the B-Mode image shown in Fig. 3a is segmented into $N = 4$ regions representing the subcutaneous fat layer (SF), the rectus abdominis muscle (M), the post peritoneal fat layer (PF) and the liver (L). For each segment k, a segmentation matrix $\mathbf{R}_k$ is created where the entries are set to a value r within the segments and 0 outside (see Fig. 3 b). From these segmentation matrices, a matrix $\mathbf{K}$ is generated:

$$\mathbf{K} = \left[\sum_{k=1}^{N} vec(\mathbf{R}_k) vec(\mathbf{R}_k)^T\right] \tag{15}$$

where not zero, the elements $\mathbf{K}(i, j) = r^2$ denote the expected correlation of the SoS between the pixels i and j. This correlation is from now on expressed in the more intuitive correlation coefficient $\rho = r^2$. Since the segments are generated with the purpose to represent different tissue regions, typically a high correlation of SoS is expected within a segment. Therefore, whenever nothing else is mentioned, ρ was set to 0.9 for the intra-segment correlation ($r = \sqrt{0.9}$). Note that the correlation between pixels across different segments is 0 (per the definition of K via the matrices R).

Finally, the covariance matrix $\mathbf{C}_M$ is formulated as follows:

$$\mathbf{C}_M(i, j) = \begin{cases} \sigma_S^2 & \text{if } i = j \\ \mathbf{K}(i, j)\sigma_S^2 & \text{else} \end{cases} \tag{16}$$

Note that the case $i = j$ in Eq. 16 accounts for the fact that the correlation of a pixel with itself is 1. σ_S designates the average variation of the estimated slowness deviation Δs from the a
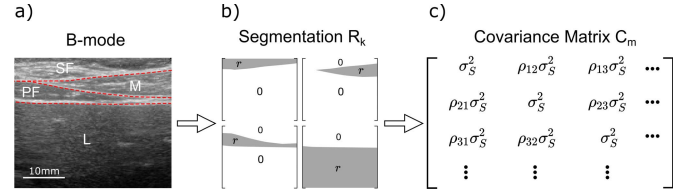

Fig. 3. Sketch of the segmentation process: (a) The B-Mode image is segmented by hand into the different tissue regions within which a correlated SoS is expected. Here, the segments represent the subcutaneous fat layer (SF), the rectus abdominis muscle (M), the post peritoneal fat layer (PF) and the liver(L). (b) Each k-th segment is represented in a corresponding segmentation matrix R_k, where the entries are set to a value r within the segments and 0 outside. (c) The R_k are then used to construct the covariance matrix C_m, where the expected correlation between pixels is described by the coefficient $\rho = r^2$. In case of no correlation of SoS (not in the same segment), the correlation coefficient ρ is 0. σ_S describes the expected average variation of the slowness deviation from *a priori* slowness deviation Δs_p.

priori slowness deviation Δs_p. σ_S is expressed in the units of slowness but can be related to the more intuitive unit of SoS by using Eq. 7:

$$\sigma_C \cong \sigma_S c_0^2 \tag{17}$$

The *a priori* information that is encoded into the parameter estimation is considered "soft" because it does not force the estimated slowness deviation inside a segment to be constant. Rather, SoS variations within the predefined segments are regularized, but not across the boundaries. Thus, in line with e.g. [41]–[43], we refer to this regularization as "soft-prior regularization", i.e. "SP regularization".

C. Synthetic Dataset

The two regularization methods were compared in a simulation study that contained various digital phantoms (DP) of different geometries (see. Fig. 6 top row) with a depth and width of 40 mm. DP 1 to DP 4 represent phantoms with inclusions of different shapes (SoS 1570 ms^{-1}) embedded in a homogeneous background (SoS 1540 ms^{-1}). DP 5 to 8 mimic layered structures as one would expect when scanning the liver through the abdomen. In DP 5 and 6, the SoS of the top layer was 1490 ms^{-1} (mimicking fat tissue) and the SoS of the bottom layer 1570 ms^{-1} (mimicking liver tissue). In addition to DP 5 and 6, DP 7 and 8 contained a triangular shaped layer embedded into the top layer with a SoS of 1585 ms^{-1} (mimicking muscle tissue). Further, DP 5 and 8 contained a circular inclusion embedded in the bottom layer with a SoS of 1600 ms^{-1} (mimicking a cancer).

Simulation of the echo shift that would be caused by these phantoms was based on determining the aberration delay using the hybrid angular spectrum approach [44], and on linking the aberration delay to echo shift using the forward model described in [29]. The advantage of the hybrid angular spectrum approach compared to other approaches is that – while being computationally efficient – it accounts for refraction/diffraction. This allows one to observe whether specific artefacts are to be expected due to the deviation of true sound propagation from the straight-ray approximation used in SoS

reconstruction. The phase noise that is typically observed in-vivo was mimicked by adding uncorrelated phase shift variations, following a Gaussian distribution with a standard deviation of 0.9 rad and a mean of 0 rad. In-vivo, the phase noise that contaminates the phase shift might change during examination (e.g. when changing the transducer position slightly). To mimic this situation, three different realizations of the synthetic phase noise were generated, henceforth termed as noise 1 to 3.

D. Phantom Design

The goal of the phantom study was to investigate the performance of both regularization approaches in a scenario mimicking an actual clinical application, namely imaging the liver through the abdominal wall, but where the actual ground truth of the SoS distribution is known. For this purpose, three phantoms that mimic the abdominal wall and liver tissue were produced. These phantoms were composed of the following compartments: a subcutaneous fat-mimicking layer (C1), a triangular-shaped muscle-mimicking layer (C2) and a post peritoneal fat-mimicking layer (C3), stacked on top of a liver-mimicking compartment (C4$_{A,B,C}$). These liver-mimicking compartments exhibit various different SoS values (see Fig. 4a) that simulate the decrease of SoS due to the increase of the liver fat fraction at different stages of fatty liver disease. The individual phantom compartments were based on porcine gelatin (Geistlich Spezial Gelatine, health and life AG, Switzerland). Three different gelatin base solutions were prepared by dissolving 10, 20 and 30 wt% porcine gelatin in H$_2$O at a temperature of 75° C. To provide a diffuse echogenecity, 2 wt% cellulose (Sigmacell Cellulose Type 20, Sigma Aldrich, Switzerland) were mixed into the base solutions. The muscle compartment (C2) was produced from the 30 wt% base solution, providing a SoS of 1585 ms^{-1} after gelling at room temperature (21 °C). Three different liver compartments (C4$_{A,B,C}$) were produced from the three different base solutions, resulting in a SoS (after gelling at room temperature) of 1525 ms^{-1}, 1555 ms^{-1} and 1585 ms^{-1}, respectively. To mimic the fat compartments in the abdominal wall, medium-chain triglycerides (MCT) oil (Ceres-MCT Oil, Puravita, Switzerland, SoS = 1350 ms^{-1}) was slowly blended under the gelatine base solution (20 wt%, not gelled yet, at a temperature of 65 ° C). During this process, an oil in gelatin emulsion was formed [45]–[48]. After gelling, the oil droplets were trapped within the gelatine matrix. The final SoS of such an emulsion is determined by the emulsion's relative MCT oil weight content, in this study 0.33 wt%, resulting in a SoS of 1490 ms^{-1} (at room temperature). The mentioned reference SoS values were determined with a through-transmission time-of-flight set-up, having an accuracy of ± 5 ms^{-1}.

E. In-Vivo Data

The two regularization techniques were examined in an exemplary case of imaging the liver of a healthy volunteer (male, age 31, in compliance with the ethical principles of the Declaration of Helsinki 2018). In comparison to the simulation
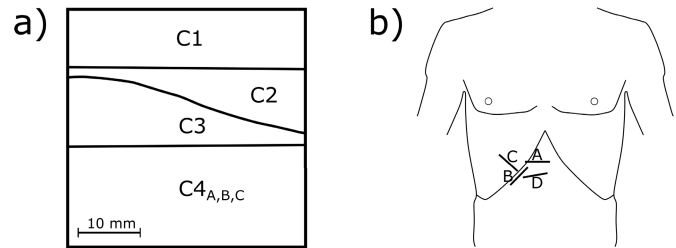

Fig. 4. (a) Sketch of the phantom geometry mimicking the abdominal wall and liver tissue: subcutaneous fat mimicking layer (C1, SoS = 1490 ms^{-1}), triangular shaped muscle (C2, SoS = 1585 ms^{-1}), post peritoneal fat layer (C3, SoS = 1490 ms^{-1}), liver mimicking compartment (C4$_{A,B,C}$, SoS = [1525 ms^{-1}, 1555 ms^{-1} and 1585 ms^{-1}]). (b) Sketch of the different scanning locations from where the liver was accessed.

and phantom study where the performance of the regularization approaches was assessed by comparing the SoS images to a ground truth, no such reference exists for the liver in the investigated in-vivo scenario. Instead, the reproducability of the SoS images was investigated by imaging the liver from various different scanning locations (see. Fig. 4b).

F. Ultrasound System

For the experimental study, a Vantage 64 LE (Verasonics Inc., WA, USA) research US system in combination with an L7-4 linear vascular probe (ATL Philips, WA, USA) was used for the pulse-echo signal acquisition. The probe features a bandwidth from 4 to 7 MHz with 5 MHz center frequency, 128 elements at 0.29 mm pitch resulting in an aperture length of 38.4 mm. The system was connected via a PCI Express link to a host computer, facilitating real time data transfer. For the acquisition of plane wave pulse-echo data, a dedicated scan sequence was implemented as described in detail in [29]. In this study, the acquired data were stored on the host computer for an off-line SoS reconstruction that was implemented in MATLAB® (MathWorks inc.).

III. RESULTS

A. Simulation Study

In both regularization methods, the outcome can be tuned via the choice of the regularization parameters. The choice of the regularization parameters is therefore crucial in view of a comparison between the two methods. For a fair comparison, we have chosen to use for each regularization method the 'optimal' set of parameters that minimizes the root-mean-square error metric.

The optimization analysis was performed as a grid search by reconstructing SoS images for all DP's and noise realizations (see Sec. II-C) with a variety of regularization parameter settings. The averaged RMSE (over all DP's and noise realizations) as a function of regularization parameter values are shown in Fig. 5. The smallest RMSE are marked with a yellow cross and the corresponding parameters are summarized in table I.

The SoS images of all DP's and noise realizations reconstructed with these sets of optimal regularization parameters are shown in Fig. 6.

TABLE I
REGULARIZATION PARAMETERS THAT LEAD TO THE SMALLEST MEAN
RMSE AMONG ALL DP'S AND NOISE REALIZATIONS

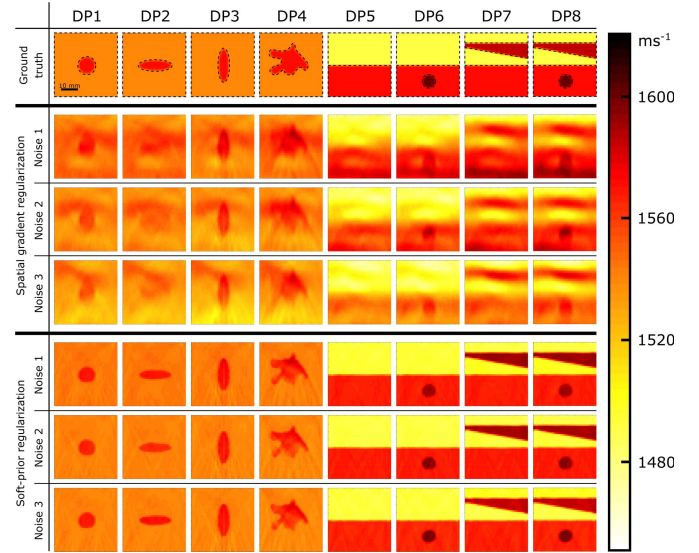|	Optimal regularization parameters	Mean RMSE
Spatial gradient	$\gamma_x = 84.1$, $\gamma_z = 17.6$	10.89 ms^{-1}
Soft-prior	$\sigma_C = 50$ ms^{-1}, $\sigma_N = 1.5$ rad	3.42 ms^{-1}
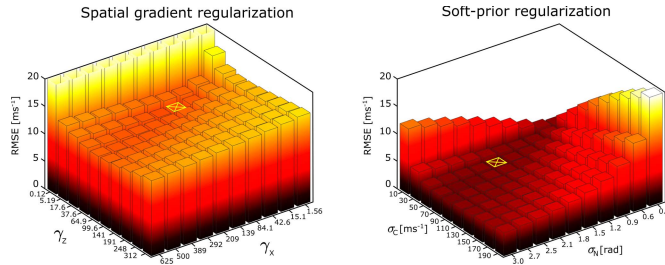
Fig. 5. Mean RMSE over all DP's and noise realizations as a function of regularization parameters. The sets of parameters that lead to the smallest mean RMSE are marked with yellow crosses.

Fig. 6. Simulation results: SoS images reconstructed with both regularization methods using the optimal set of regularization parameters and three different realizations of the phase noise. The top row shows the ground truth. The scale bar corresponds to 10 mm.

Fig. 7. SoS images of DP 4 using circular segmentations with various different radii and three different correlation coefficients ρ. Whereas for ρ close to 1, misleading segmentations lead to strong artifacts in the SoS image, lower values of ρ allow a better perception of the true structure in the DP. The scale bar corresponds to 10 mm.

The SoS images that were reconstructed with the SG regularization show strong artifacts in all DP's. These artifacts mimic SoS variations that bias the ground truth and further impede an unambiguous identification of the SoS inclusions. The spatial distribution of these artifactual SoS variations changes among the different noise realizations but is rather constant across the different DP geometries. Further, the mean SoS within the segments are strongly influenced by the phase noise: whereas e.g. the mean SoS of the liver mimicking segment in the DP's 5 to 8 deviate only little from the ground truth with noise 1, they strongly deviate in the case of noise 3. Similarly in DP 1 to 4, the SoS underneath the inclusions deviates most strongly from the ground truth in case of noise 3.

A disadvantage of the spatial gradient regularization is that it results in a trade-off between a smooth SoS distribution inside compartments and a high spatial resolution across compartment boundaries. In situations with strong phase noise, a relatively strong regularization is needed to suppress high frequency artifacts (i.e. to enforce a smooth SoS distribution). Such strong regularization, however, results in a reduced spatial resolution of the reconstructed image. This effect is strongly pronounced in DP's 5 to 8: the strong regularization that was needed to minimize RMSE by enforcing smooth SoS distributions inside the individual compartments lead to blurred transitions across different compartments.

Contrary to the SG regularization, the SP regularization allows to minimize SoS variations within the individual compartments without blurring transitions across boundaries. This results in a minimum RMSE that is more than a factor of 3 smaller in comparison to the SG regularization (see table. I). Furthermore, all the SoS images reconstructed with the SP regularization agree well with the ground truth and show hardly any differences across the different synthetic phase noises.

So far, we assumed that the location and shape of the inclusion is *a priori* known so that it can be properly segmented.
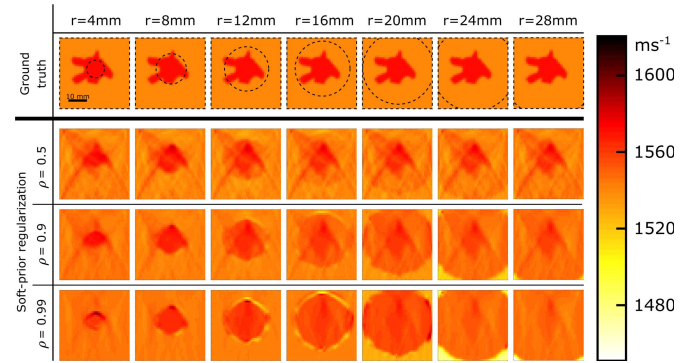
In an actual clinical scenario, however, a region of SoS contrast might not be clearly visible in the B-Mode image. This can result in three scenarios: (i) inaccurate segmentations, (ii) structures that are completely missed in the segmentation and (iii) segmentations that are overdone, i.e. by segmenting an inclusion inside a homogeneous region by accident. The first case is investigated by again reconstructing DP 4 (including phase noise realization 3), but now using circular segments of various different radii (see Fig. 7). As described in Materials and Methods, the SP regularization includes a coefficient ρ that describes the correlation of SoS between pixels within the same segment. So far, this coefficient was set to 0.9 to enforce a high correlation and therefore a smooth SoS distribution. In the following, the influence of the correlation parameter ρ on the SoS images is investigated by using various values of ρ between 0.5 and 0.99. The SoS images (see Fig. 7) show that for a value of $\rho = 0.99$, the shape of the inclusion cannot be perceived, independent of the size of the segmentation.
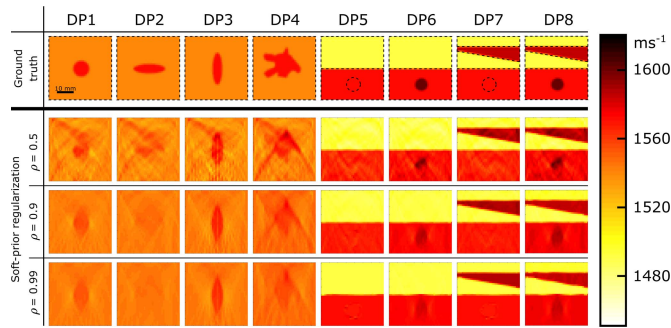
Fig. 8. Simulation results: SoS images reconstructed with the SP regularization without segmenting the inclusions. The top row shows the ground truth, where the black dashed lines indicate the segmentation. In DP5 and DP7, inclusions were segmented into the lower part where non was present in the DP. The SoS images were reconstructed with different values for the correlation coefficient ρ, based on the simulated phase shift maps including artificial phase noise 3. The scale bar corresponds to 10 mm.

Moreover, artifacts occur at the edge of the circular segment. Contrary, when decreasing the correlation coefficient ρ, the influence of the segmentation to the SoS image is weaker, resulting in a better perception of the true structure in the DP. Anyhow, independent of the size of the segmentation, the SoS contrast is underestimated by about 10 ms^{-1} for a value of $\rho = 0.5$. Furthermore, lower values of ρ lead to SoS images that are more prone to the phase noise.

To investigate the second and third scenario, the SoS images were reconstructed (including phase noise realization 3 but without segmenting the inclusions (DP1-DP4, DP6 and DP8, see Fig. 8 top row) and with inclusions segmented inside the lower compartment where none is present (DP5 and DP7, see Fig. 8 top row).

The SoS images (see Fig. 8) show that – even when the inclusions are not included as part of the *a priori* knowledge – their influence on the SoS image is well visible for most of the DP's. However, for ρ close to 1, the SoS images show a very bad axial resolution. Consequently, the inclusions in DP2 and DP4 are barely visible because they are bounded mainly by horizontal boundaries. On the contrary, the good visibility of the inclusions in DP 1,3,6 and 8 relays on the good lateral resolution in combination with the stronger prevalence of axial boundaries.

A value for ρ of 0.5 results in SoS images with a better axial resolution. This results in a better visibility of the inclusions in DP2 and DP4. On the other hand, an increased level of artifacts is observed in all DP's for such a value of ρ.

Independent of the value for ρ, segmenting an inclusion that is not present in the SoS images has only minimal effect on the reconstructed SoS images.

B. Phantom Results

As described in Materials and Methods, three phantoms were investigated that mimic the abdominal wall and the liver tissue with various different liver SoS, where P1, P2 and P3 correspond to liver mimicking compartments with SoS values of 1525 ms^{-1}, 1555 ms^{-1} and 1585 ms^{-1}, respectively. The

TABLE II
REGULARIZATION PARAMETERS THAT LEAD TO THE SMALLEST MEAN RMSE AMONG ALL PHANTOMS AND PHASE NOISES

	Optimal regularization parameters	Mean RMSE
Spatial gradient	$\gamma_x = 56.3$, $\gamma_z = 1.43$	19.17 ms^{-1}
Soft-prior	$\sigma_C = 30$ ms^{-1}, $\sigma_N = 1.5$ rad	6.17 ms^{-1}
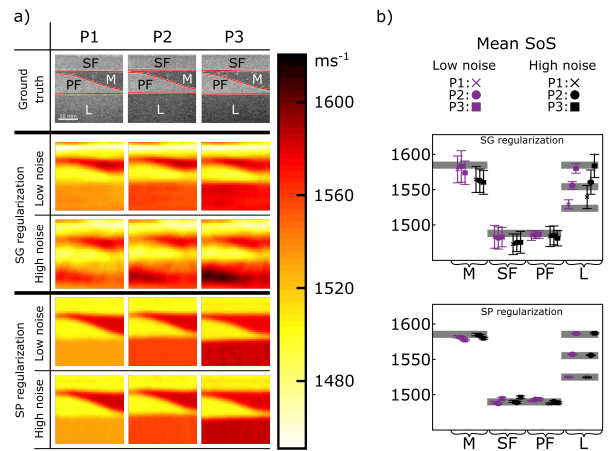
Fig. 9. Phantom results: (a) The top row shows the B-Mode images where the red lines indicate the segmentations that were used for the SP regularization. The SoS images were reconstructed from the data directly, containing only actual measurement noise (low noise) and when adding artificially generated phase noise (high noise) to closely mimic the in-vivo scenario. (b) Mean and standard deviation evaluated within individual segments. The scale bar corresponds to 10 mm.

corresponding B-Mode images are shown in Fig. 9a (top row). The red lines indicate the segments that were identified for the SP regularization. The phase shift maps of these phantoms are contaminated only by a low level of phase noise (henceforth referred as 'low noise') (see Fig. 1a for an example). In-vivo, however, a higher level of phase noise is typically observed, potentially due to a higher amount of multiple scattering processes and SoS inhomogeneities in the sub-resolution range (see Fig. 1b for an example). To closely mimic the in-vivo scenario, SoS images were not only reconstructed from the actual measurement ('low noise'), but also after adding artificially generated phase noise comparable to what can be found in vivo ('strong noise').

The digital phantoms that were used for the optimization analysis in section III-A contained not only layered but also inclusion structures. In the following, however, we specifically focus on layered samples, in view of the clinical application of liver imaging. For this reason, the optimal parameters found for the DP's are not necessarily representative for the phantom study. Therefore, a parameter optimization was again performed with the purpose to find the optimal set of regularization parameters for this particular scenario. To do so, a grid search was carried out with the goal to find the set of regularization parameters that lead to SoS images with the smallest mean RMSE over all phantoms and both, the low and high noise situation. Thereby, the RMSE was determined relative to the ground truth given by the known spatial distribution of the compartments seen on the B-mode images, in combination with the reference SoS values of the different

compartments. The sets of optimal parameters are summarized in table II. The SoS images that were reconstructed with this set of optimal parameters are shown in Fig. 9 a). To aid a quantitative assessment of the reconstructed SoS images, the mean SoS and standard deviation of each segment are shown in Fig. 9 b).

In the case of low phase noise, both regularization approaches result in SoS images that represent the true SoS distribution fairly well. The SG regularization, however, leads to a higher variation of SoS inside the different segments, reflected by the larger standard deviation in Fig. 9 b. With the SG regularization, the high noise leads to an increase in the level of artifacts, most pronounced in the L compartment. Furthermore, the stronger phase noise also biases the mean SoS of the various compartments, most pronounced in the L compartment of phantom 1 and the M compartment in all phantoms.

In case of the SP regularization, the reconstructed SoS agrees very well with the ground truth, independent of the phase noise.

C. In-Vivo Results

Since no ground truth SoS is available in-vivo, an optimization study to find the optimal regularization parameters as it has been done in the simulation and phantom experiments is difficult. Anyhow, since we explicitly designed the phantom experiment (geometry, SoS contrast, mimicked phase noise) similar to what we expect also in-vivo, the regularization parameters were chosen equal to the parameters that were already used in the phantom study (see table. II).

To investigate whether artifacts in the SoS images are caused by phase noise or by the anatomical structure (e.g. via violation of the straight-ray approximation), the liver was imaged three times for each scanning location, but with a slightly changed transducer position, thus providing images with different phase noise realisations but identical anatomy. The corresponding B-Mode images are shown in Fig. 10a, where the red lines indicate the segmentations that were used for the SP regularization. The SoS images reconstructed with the SG and SP regularization are shown directly below the corresponding B-Mode images. To aid a quantitative comparison between the SoS images, the mean SoS values inside the liver were evaluated and summarized in Fig. 10b. The standard deviations of the liver SoS of each scanning location are represented by error bars.

In case of the SG regularization, the SoS distribution inside the liver is highly non-uniform. Furthermore, the SoS distribution not only varies between different scanning locations, but also within the same scanning location (but slightly shifted transducer position). Fig. 10b reveals that the liver's mean SoS is scattered in a range of about 40 ms^{-1} among the different SoS images.

In contrast, SoS images reconstructed with the SP regularization show uniform SoS distribution inside the liver, as one would expect in a healthy volunteer. Furthermore, the mean SoS of the liver is more consistent among the different

scans, scattered in a smaller range of only about 10 ms^{-1} (see Fig. 10b bottom).

IV. DISCUSSION AND CONCLUSION

In this study, we have shown that the phase noise that is typically observed in-vivo leads to strong artifacts in the SoS images when using a Tikhonov-type regularization of the spatial gradient (SG) for solving the inverse problem. This often leads to SoS images that are not reproducible, when for example repeatedly imaging the same tissue region, and thus makes quantitative interpretation difficult. Further, the SG regularization acts across tissue boundaries. This results in a trade-off between a smooth SoS distribution inside tissue compartments and a high spatial resolution across tissue compartment boundaries. To overcome this shortcoming, we proposed to use a Bayesian framework for solving the inverse problem. One of the advantages of the Bayesian framework is that it provides a convenient and intuitive way to include an *a priori* statistical model about the distribution of SoS. We have shown in the simulation, phantom experiment and in a first in-vivo study that including geometrical *a priori* information leads to SoS images that are less noise-sensitive and thus is a key step towards quantitative and reproducible SoS imaging in echo-mode.

In the Bayesian framework, we assumed that the noise is Gaussian distributed around the prediction of the forward model. This has the advantage that the posterior probability distribution in Eq. 12 is also Gaussian and therefore allows a computationally efficient determination of the most likely solution. However, the phase shift maps in Fig. 1 suggest that this approximation is not entirely true. For example, the phase shift map at the right lower corner shows phase noise that follows more a salt-and-pepper distribution than a Gaussian distribution. Anyway, the SoS images show that a Gaussian approximation still results in accurate reproducible SoS images. Further work will focus on the influence of the noise distribution to the SoS images.

The identification of the tissue segments that were part of the *a priori* model were derived from the B-Mode images, by visually segmenting the different tissue regions. In phantoms, segmentation was not difficult since they consisted of well defined compartments. In-vivo, however, clutter and aberration can result in B-Mode images where a proper identification of certain tissue regions, such as e.g. cancer, might be difficult. In a clinical situation, the accuracy of the segmentation could be improved if high resolution images obtained from other modalities such as computer tomography of magnetic resonance imaging can be used as *a priori* knowledge. Independent of the method of segmentation, the simulations nevertheless revealed that even SoS inhomogeneities that are not properly segmented can be reconstructed when explicitly allowing pixel-wise SoS variations via a choice of ρ smaller than one. On the other hand, a reduced pixel-wise correlation results in SoS images that are more prone to phase noise. This drawback could be circumvented by reducing the phase noise in a first place. Possible approaches might be to use already established techniques that increase the B-Mode image quality
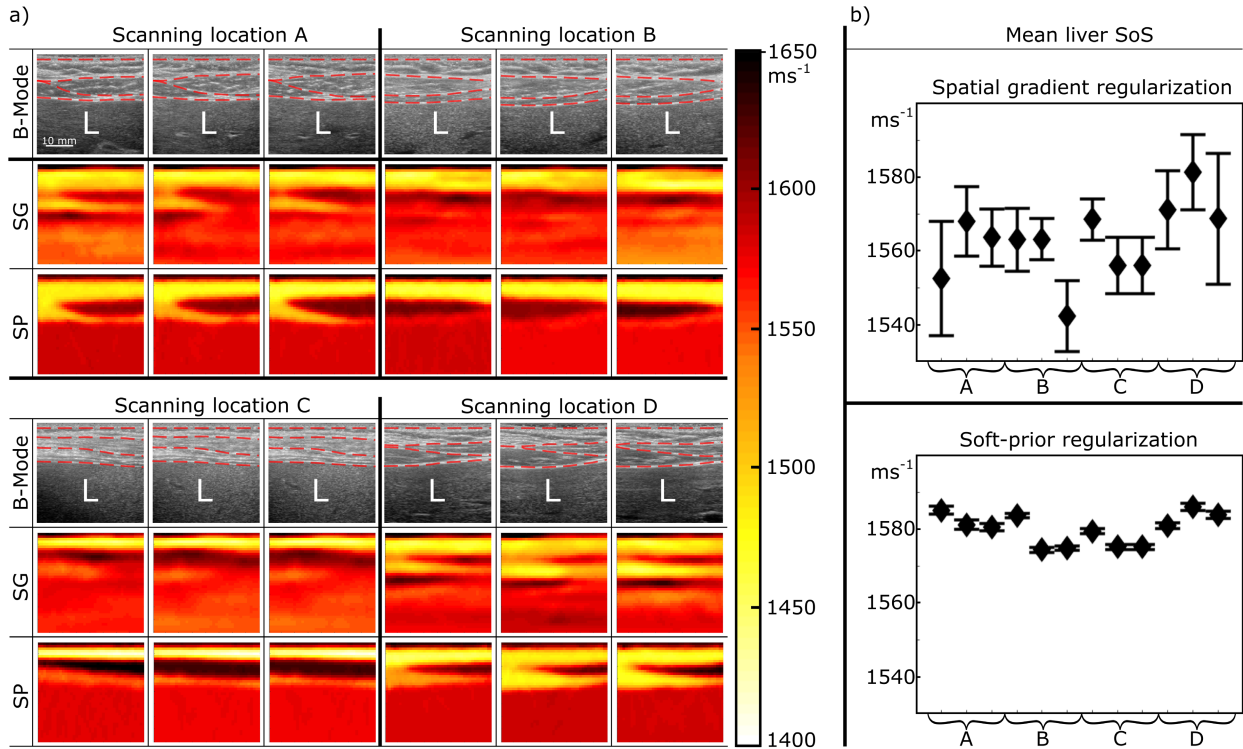
Fig. 10.   (a) In-vivo SoS images when accessing the liver from four different scanning locations. At each scanning location, three images were acquired with a slightly changed transducer position. The segmentation that were used for the SP regularization are indicated in the B-Mode images by the red dashed lines. (b) Mean SoS and standard deviation of the liver (L) from different scanning location.

such as for example frequency compounding or second harmonic imaging. Recently, an approach has been proposed that focuses at distinct points in emission and reception to build a reflection matrix containing the impulse responses between a set of virtual transducers mapping the entire medium [49]. This allows to apply a local focusing criterion that enables to evaluate the image quality anywhere inside the medium. This approach might be used to identify image regions within which noise is predominant and therefore, no relevant phase information is available. These regions could then be excluded in the formulation of the forward model.

One important assumption made in this study was the straight ray approximation of US propagation. Although this assumption neglects diffraction and refraction effects, our results demonstrate that the straight ray approximation was reasonable in the investigated scenarios (i.e segment geometries and SoS contrast levels) in the sense that correct quantitative results could be obtained. The straight ray approximation has, however, the invaluable advantage that the forward model is linear and can be formulated in matrix notation. Thus, real-time imaging can be obtained when using the SG regularization by pre-calculating the computationally expensive term $\left(\mathbf{M}^T\mathbf{M} + \mathbf{T}^T\mathbf{T}\right)^{\text{inv}}$. In the SP approach, a pre-calculation of the posterior covariance matrix is more difficult since it depends on the tissue segmentation which is in principle only available at the time of data acquisition. Moreover, the presented method relies on a manual segmentation of the B-Mode images and thus impedes real-time imaging. Another concern might be that manual segmentation might be not practical

in a clinical environment. State-of-the-art US devices are, however, equipped with easy-to-use graphical user interfaces that allow a quick and easy manual segmentation of various anatomical features. For example, in the field of obstetric care, it is the state-of-the-art method to manually segment the scull, the femur etc. for estimating the fetal age. Anyhow, manual segmentation can be a time-consuming task, which in addition requires expert knowledge. Therefore, future work will focus on the replacement of the manual segmentation with a technique that is able to extract the relevant information form the B-Mode images automatically. This could be done by applying machine learning based approach such as [50]–[52].

The regularization techniques are evaluated in-vivo at the example of imaging the liver. This organ was chosen because it is easy to access from various different scanning locations, providing different geometries of the overlying tissue structures. Rather than the linear probe that was used in this study, curvilinear probes are usually preferred for this application. These kind of probes typically feature a lower center frequency allowing larger imaging depth, thus better matching the size of the liver. CUTE can be readily adapted to such probes. However, one has to keep in mind that the ratio between the probe aperture length and the required depth range for full liver imaging limits the available angle range, resulting in a reduced axial resolution in comparison to superficial tissue. This reduced axial resolution might, however, be compensated with the SP regularization. Anyway, even if the full depth of the liver may not be reached, CUTE can be a valuable tool for liver diagnosis.

Although further clinical evidence is required to draw medically relevant conclusions, the high accuracy of the SoS reconstruction in the phantom results as well as the reproducibility in the in-vivo results are very promising for the diagnosis of fatty liver disease. It has been reported that the mean liver SoS decreases on average by about 40 ms^{-1} in a liver having steatosis of grade 1 (according to the Brunt scale) compared to a healthy liver [26], [27]. This underlines the value of the SP regularization for improving the diagnostic sensitivity of CUTE in fatty liver disease. Apart from liver imaging, a broad range of potential applications for CUTE can be envisaged, as e.g. the diagnosis of cancer or the assessment of plaque inside the carotid artery.

DATA AVAILABILITY

The experimental data used in this study are available on request from M. Frenz.

REFERENCES

[1] J. A. Baker, P. J. Kornguth, M. S. Soo, R. Walsh, and P. Mengoni, "Sonography of solid breast lesions: Observer variability of lesion description and assessment," *Amer. J. Roentgenology*, vol. 172, no. 6, pp. 1621–1625, Jun. 1999.

[2] K. Konno *et al.*, "Liver tumors in fatty liver: Difficulty in ultrasonographic interpretation," *Abdominal Imag.*, vol. 26, no. 5, pp. 487–491, Sep. 2001.

[3] G. Rahbar *et al.*, "Benign versus malignant solid breast masses: US differentiation," *Radiology*, vol. 213, no. 3, pp. 889–894, Dec. 1999.

[4] A. Athanasiou *et al.*, "Breast lesions: Quantitative elastography with supersonic shear imaging—Preliminary results," *Radiol.*, vol. 256, no. 1, pp. 297–303, 2010.

[5] J. Bamber *et al.*, "EFSUMB guidelines and recommendations on the clinical use of ultrasound Elastography—Part 1: Basic principles and technology," *Ultraschall der Medizin Eur. J. Ultrasound*, vol. 34, no. 2, pp. 169–184, Apr. 2013.

[6] R. G. Barr, "Real-time ultrasound elasticity of the breast: Initial clinical results," *Ultrasound Quart.*, vol. 26, no. 2, pp. 61–66, Jun. 2010.

[7] D. Cosgrove *et al.*, "EFSUMB guidelines and recommendations on the clinical use of ultrasound elastography—Part 2: Clinical applications," *Ultraschall Med*, vol. 34, no. 3, pp. 238–253, 2013.

[8] C. Dietrich *et al.*, "EFSUMB guidelines and recommendations on the clinical use of liver ultrasound elastography, update 2017 (Long Version)," *Ultraschall der Medizin Eur. J. Ultrasound*, vol. 38, no. 4, p. e48, Aug. 2017.

[9] R. M. Sigrist, J. Liau, A. El Kaffas, M. C. Chammas, and J. K. Willmann, "Ultrasound elastography: Review of techniques and clinical applications," *Theranostics*, vol. 7, no. 5, p. 1303, 2017.

[10] S. Hu and L. V. Wang, "Photoacoustic imaging and characterization of the microvasculature," *J. Biomed. Opt.*, vol. 15, no. 1, 2010, Art. no. 011101.

[11] M. Jaeger, "Deformation-compensated averaging for clutter reduction in epiphotoacoustic imaging *in vivo*," *J. Biomed. Opt.*, vol. 17, no. 6, Jun. 2012, Art. no. 066007.

[12] K. G. Held, M. Jaeger, J. Rička, M. Frenz, and H. G. Akarçay, "Multiple irradiation sensing of the optical effective attenuation coefficient for spectral correction in handheld OA imaging," *Photoacoustics*, vol. 4, no. 2, pp. 70–80, Jun. 2016.

[13] L. Ulrich *et al.*, "Spectral correction for handheld optoacoustic imaging by means of near—Infrared optical tomography in reflection mode," *J. Biophotonics*, vol. 12, no. 1, 2018, Art. no. e201800112.

[14] J. Wiskin, D. T. Borup, S. A. Johnson, and M. Berggren, "Non-linear inverse scattering: High resolution quantitative breast tissue tomography," *J. Acoust. Soc. Amer.*, vol. 131, no. 5, pp. 3802–3813, May 2012.

[15] G. Y. Sandhu, C. Li, O. Roy, S. Schmidt, and N. Duric, "Frequency domain ultrasound waveform tomography: Breast imaging using a ring transducer," *Phys. Med. Biol.*, vol. 60, no. 14, p. 5381, 2015.

[16] J. Wiskin, B. Malik, R. Natesan, and M. Lenox, "Quantitative assessment of breast density using transmission ultrasound tomography," *Med. Phys.*, vol. 46, no. 6, pp. 2610–2620, Jun. 2019.

[17] R. Natesan, J. Wiskin, S. Lee, and B. H. Malik, "Quantitative assessment of breast density: Transmission ultrasound is comparable to mammography with tomosynthesis," *Cancer Prevention Res.*, vol. 12, no. 12, pp. 871–876, Dec. 2019.

[18] J. Wiskin, B. Malik, V. Theendakara, and J. Klock, "Orthopedic and myopathic imaging with transmission ultrasound tomography: Experimental verification, quantitative accuracy and clinical implications," *Proc. SPIE*, vol. 11319, Mar. 2020, Art. no. 113190W.

[19] M. Kondo, K. Takamizawa, M. Hirama, K. Okazaki, K. Iinuma, and Y. Takehara, "An evaluation of an *in vivo* local sound speed estimation technique by the crossed beam method," *Ultrasound Med. Biol.*, vol. 16, no. 1, pp. 65–72, Jan. 1990.

[20] I. Céspedes, J. Ophir, and Y. Huang, "On the feasibility of pulse-echo speed of sound estimation in small regions: Simulation studies," *Ultrasound Med. Biol.*, vol. 18, no. 3, pp. 283–291, Jan. 1992.

[21] M. C. Hesse, L. Salehi, and G. Schmitz, "Nonlinear simultaneous reconstruction of inhomogeneous compressibility and mass density distributions in unidirectional pulse-echo ultrasound imaging," *Phys. Med. Biol.*, vol. 58, no. 17, p. 6163, 2013.

[22] M. Jakovljevic, S. Hsieh, R. Ali, G. Chau Loo Kung, D. Hyun, and J. J. Dahl, "Local speed of sound estimation in tissue using pulse-echo ultrasound: Model-based approach," *J. Acoust. Soc. Amer.*, vol. 144, no. 1, pp. 254–266, Jul. 2018.

[23] S. J. Sanabria, E. Ozkan, M. Rominger, and O. Goksel, "Spatial domain reconstruction for imaging speed-of-sound with pulse-echo ultrasound: Simulation and *in vivo* study," *Phys. Med. Biol.*, vol. 63, no. 21, Oct. 2018, Art. no. 215015.

[24] L. Ruby *et al.*, "Breast cancer assessment with pulse-echo speed of sound ultrasound from intrinsic tissue reflections: Proof-of-concept," *Investigative Radiol.*, vol. 54, no. 7, pp. 419–427, Jul. 2019.

[25] A. S. Podkowa and M. L. Oelze, "The convolutional interpretation of registration-based plane wave steered pulse-echo local sound speed estimators," *Phys. Med. Biol.*, vol. 65, no. 2, Jan. 2020, Art. no. 025003.

[26] M. Imbault *et al.*, "Robust sound speed estimation for ultrasound-based hepatic steatosis assessment," *Phys. Med. Biol.*, vol. 62, no. 9, p. 3582, 2017.

[27] M. Dioguardi Burgio *et al.*, "Ultrasonic adaptive sound speed estimation for the diagnosis and quantification of hepatic steatosis: A pilot study," *Ultraschall der Medizin Eur. J. Ultrasound*, vol. 40, no. 6, pp. 722–733, Dec. 2019.

[28] M. Jaeger, G. Held, S. Peeters, S. Preisser, M. Grünig, and M. Frenz, "Computed ultrasound tomography in echo mode for imaging speed of sound using pulse-echo sonography: Proof of principle," *Ultrasound Med. Biol.*, vol. 41, no. 1, pp. 235–250, Jan. 2015.

[29] P. Stähli, M. Kuriakose, M. Frenz, and M. Jaeger, "Improved forward model for quantitative pulse-echo speed-of-sound imaging," *Ultrasonics*, vol. 108, Dec. 2020, Art. no. 106168.

[30] T. Loupas, J. T. Powers, and R. W. Gill, "An axial velocity estimator for ultrasound blood flow imaging, based on a full evaluation of the Doppler equation by means of a two-dimensional autocorrelation approach," *IEEE Trans. Ultrason., Ferroelectr., Freq. Control*, vol. 42, no. 4, pp. 672–688, Jul. 1995.

[31] C. Kasai, K. Namekawa, A. Koyano, and R. Omoto, "Real-time two-dimensional blood flow imaging using an autocorrelation technique," *IEEE Trans. Sonics Ultrason.*, vol. 32, no. 3, pp. 458–464, May 1985.

[32] A. Tarantola and B. Valette, "Generalized nonlinear inverse problems solved using the least squares criterion," *Rev. Geophys.*, vol. 20, no. 2, pp. 219–232, 1982.

[33] M. Jaeger and M. Frenz, "Quantitative imaging of speed of sound in echo ultrasonography," in *Proc. IEEE Int. Ultrasound Symp.*, Taipei, Taiwan, Oct. 2015, pp. 320–321, Paper 4G-2.

[34] W. P. Gouveia and J. A. Scales, "Bayesian seismic waveform inversion: Parameter estimation and uncertainty analysis," *J. Geophys. Res., Solid Earth*, vol. 103, no. B2, pp. 2759–2779, Feb. 1998.

[35] A. Malinverno, "A Bayesian criterion for simplicity in inverse problem parametrization," *Geophys. J. Int.*, vol. 140, no. 2, pp. 267–285, Feb. 2000.

[36] K. Mosegaard and A. Tarantola, "Monte Carlo sampling of solutions to inverse problems," *J. Geophys. Res., Solid Earth*, vol. 100, no. B7, pp. 12431–12447, Jul. 1995.

[37] A. P. Valentine and M. Sambridge, "Optimal regularization for a class of linear inverse problem," *Geophys. J. Int.*, vol. 215, no. 2, pp. 1003–1021, Nov. 2018.

[38] F. M. Hooi and P. L. Carson, "First-arrival traveltime sound speed inversion with *a priori* information," *Med. Phys.*, vol. 41, Jul. 2014, Art. no. 082902.

[39] P. Stahli, M. Frenz, and M. Jaeger, "Reflection-mode speed-of-sound imaging using soft-prior limits," in *Proc. IEEE Int. Ultrason. Symp. (IUS)*, Oct. 2019, pp. 948–950.

[40] A. Tarantola, *Inverse Problem Theory Methods for Model Parameter Estimation*, vol. 89. Philadelphia, PA, USA: SIAM, 2005.

[41] A. Golnabi, S. Geimer, P. Meaney, and K. Paulsen, "Comparison of no-prior and soft-prior regularization in biomedical microwave imaging," *J. Med. Phys.*, vol. 36, no. 3, p. 159, 2011.

[42] M. McGarry *et al.*, "Including spatial information in nonlinear inversion MR elastography using soft prior regularization," *IEEE Trans. Med. Imag.*, vol. 32, no. 10, pp. 1901–1909, Oct. 2013.

[43] J. Feng *et al.*, "Direct soft prior regularization in NIR spectral tomography from MRI-contrast and distance-constraints, for segmentation-free reconstruction," in *Cancer Imag. Therapy OSA Tech. Dig.*, Fort Lauderdale, FL, USA, Apr. 2016, Paper JM3A.4.

[44] U. Vyas and D. Christensen, "Ultrasound beam simulations in inhomogeneous tissue geometries using the hybrid angular spectrum method," *IEEE Trans. Ultrason., Ferroelectr., Freq. Control*, vol. 59, no. 6, pp. 1093–1100, Jun. 2012.

[45] E. L. Madsen, J. A. Zagzebski, and G. R. Frank, "An anthropomorphic ultrasound breast phantom containing intermediate-sized scatteres," *Ultrasound Med. Biol.*, vol. 8, no. 4, pp. 381–392, Jan. 1982.

[46] E. L. Madsen, G. R. Frank, T. A. Krouskop, T. Varghese, F. Kallel, and J. Ophir, "Tissue-mimicking Oil-in-Gelatin dispersions for use in heterogeneous elastography phantoms," *Ultrason. Imag.*, vol. 25, no. 1, pp. 17–38, Jan. 2003.

[47] E. L. Madsen *et al.*, "Anthropomorphic breast phantoms for testing elastography systems," *Ultrasound Med. Biol.*, vol. 32, no. 6, pp. 857–874, Jun. 2006.

[48] M. M. Nguyen, S. Zhou, J.-L. Robert, V. Shamdasani, and H. Xie, "Development of oil-in-gelatin phantoms for viscoelasticity measurement in ultrasound shear wave elastography," *Ultrasound Med. Biol.*, vol. 40, no. 1, pp. 168–176, Jan. 2014.

[49] W. Lambert, L. A. Cobus, M. Couade, M. Fink, and A. Aubry, "Reflection matrix approach for quantitative imaging of scattering media," 2019, *arXiv:1911.03147*. [Online]. Available: http://arxiv.org/abs/1911.03147

[50] Q. Huang, Y. Luo, and Q. Zhang, "Breast ultrasound image segmentation: A survey," *Int. J. Comput. Assist. Radiol. Surg.*, vol. 12, no. 3, pp. 493–507, Mar. 2017.

[51] H. B. Kekre and P. Shrinath, "Tumour delineation using statistical properties of the breast US images and vector quantization based clustering algorithms," *Int. J. Image, Graph. Signal Process.*, vol. 5, no. 11, pp. 1–12, Sep. 2013.

[52] N. Torbati, A. Ayatollahi, and A. Kermani, "An efficient neural network based method for medical image segmentation," *Comput. Biol. Med.*, vol. 44, pp. 76–87, Jan. 2014.